Electronic structure calculations and determination of related properties for radium

Aryan Iden Khojandi[1] and D. A. Papaconstantopoulos[2]
[1]*Thomas Jefferson High School for Science and Technology, Alexandria, Virginia 22312, USA*
[2]*Department of Computational and Data Sciences, George Mason University, Fairfax, Virginia 22030, USA*
(Received 3 November 2009; revised manuscript received 21 August 2010; published 14 October 2010)

We employed density-functional theory using a scalar-relativistic approach to perform self-consistent electronic structure calculations for the heavy element radium in the fcc, bcc, hcp, and sc structures. Our calculations using the linearized augmented plane wave method in the generalized gradient approximation with a sufficiently dense *k*-point mesh predicted the bcc as the ground-state structure and equilibrium lattice parameter in excellent agreement with experiment, whereas the local density approximation found the incorrect ground-state structure and underestimated the equilibrium lattice parameter. We also calculated the elastic constants and related moduli in order to explore the mechanical properties of radium. We further investigated the density of states and band structure of both bcc and fcc radium, at ambient conditions, in the expanded lattice, and under high pressure, and found results similar to those found for other alkaline earth metals with the corresponding structures as their ground states. Additionally, we used our total-energy and enthalpy results to predict a phase transition from bcc to fcc at a pressure of about 2.0 GPa. We then employed McMillan's theory of superconductivity, discovering increased superconducting temperatures for both structures under pressure and a superconductivity transition temperature of about 10 K for the fcc structure under a pressure of 16.9 GPa. We also present results in which we included spin-orbit interactions, which show small effects.

DOI: 10.1103/PhysRevB.82.155121 PACS number(s): 31.15.−p, 62.20.−x

I. INTRODUCTION

Despite its unique and interesting properties, radium, the heaviest of the alkaline earth metals, has remained a relatively unstudied element throughout the years, at least insofar as its electronic structure and related properties are concerned. This relative lack of exploration of the electronic properties of radium can be attributed, in the experimental sense, to its scarcity, its radioactivity, and its tendency to oxidize quickly upon exposure to air. However, nor has any theoretical research hitherto been conducted regarding the electronic structure and related properties of Radium. We suspect that this results from the softness of the material, causing extremely small differences in volume variations of the total energy, which render the convergence of self-consistent calculations difficult. Indeed, the first two columns of the Periodic Table, where the energy differences between different volumes are very small, have been known to cause difficulties for density-functional theory (DFT). Therefore, successful results from DFT calculations for radium represent an expanded use of DFT for both very soft materials and materials with high atomic numbers, thereby making DFT, in the way that we have employed it, a powerful tool applicable across the Periodic Table. Furthermore, the predicted superconducting properties represent a test and an application of McMillan's theory of superconductivity, where the electron-phonon interaction is the accepted mechanism. They also represent progress on a significant question that has been of interest to scientists since the discovery of superconductivity: can materials that are not known to superconduct under ambient conditions be turned into superconductors by the application of pressure, and at what temperature. We employed the DFT of Hohenberg-Kohn-Sham.[1,2] In this paper, we report the results of the first set of band structure calculations using the augmented-plane-wave (APW) method both in its muffin-tin (MT) approximation and its full-potential linearized (LAPW) forms. Most of our calculations followed the scalar-relativistic approach; that is, in solving the Schrödinger equation we included the mass-velocity and Darwin relativistic corrections, but we neglected the spin-orbit coupling for the valence states. We performed additional calculations including the spin-orbit and found small differences. We originally employed the local-density approximation (LDA), but then opted to use the generalized gradient approximation (GGA) (Ref. 3) for treating exchange and correlation in order to obtain more accurate results for equilibrium lattice parameters. Specifically, we present calculations of the total energy as a function of volume for the bcc, fcc, hcp, and sc structures. These calculations allowed us to determine the ground state to correspond to the bcc lattice and the equilibrium lattice parameter in very good agreement with the measured value. In addition, we predict values for the elastic constants and present diagrams for the energy bands and density of states (DOS). We used our densities of states and their angular momentum components at the Fermi level to determine the electron-phonon interaction and make predictions of possible superconductivity occurring under high pressures. Also, from our enthalpy calculations we predict a phase transition from bcc to fcc. This study, to the best of our knowledge, is the first set of electronic structure calculations for radium.

II. THEORY AND COMPUTATIONAL DETAILS

A. Total energies

Full-potential self-consistent scalar relativistic LAPW total-energy calculations[4,5] were performed for radium to determine the relationships between energy, pressure, and volume. In our calculations, the core states were treated as fully

TABLE I. Calculated lattice constants and bulk moduli of bcc and fcc Radium and the corresponding energy differences between the two structures. (Note: LAPW GGA FINAL refers to the calculations done with 819 bcc and 1469 fcc k points, RK_{max} increased to 10.5, and a denser radial mesh of 900 points in the muffin-tin sphere.)

	bcc		fcc		
Method	Lattice constant a (bohr)	Bulk modulus B (GPa)	Lattice constant a (bohr)	Bulk modulus B (GPa)	$\Delta E=E_{fcc}-E_{bcc}$ (Ry)
MT-APW LDA 55/89	9.11		11.59		-1.1×10^{-2}
LAPW LDA 55/89	9.35	10.18	11.79	8.95	-7.0×10^{-5}
LAPW LDA 285/505	9.37	9.46	11.80	9.28	-5.0×10^{-5}
LAPW GGA 55/89	9.81	8.00	12.45	7.21	1.9×10^{-3}
LAPW GGA 285/505	9.86	7.57	12.45	7.23	8.0×10^{-5}
LAPW GGA 819/1469	9.86	7.45	12.45	7.29	7.0×10^{-5}
LAPW GGA FINAL	9.82	7.57	12.41	7.25	9.0×10^{-5}
Expt.	9.73[a]				

[a]Reference 17.

relativistic while the 6*p* and 7*s* states were treated as semirelativistic. We used the LDA version of Hedin-Lundqvist[6] as well as the Perdew-Wang GGA (Ref. 3) approach for approximating exchange and correlation. In the LAPW calculations, the total energies were iterated to self-consistency until they differed by less than 10^{-5} Ry. A muffin-tin sphere of radius 3.4 a.u. was used for all structures and lattice constants in the LDA and GGA total-energy calculations. Once converged, the 6*p* semicore charge density contained less than 0.02 electrons outside the MT sphere. The RK_{max} value, in which R is the radius of the muffin-tin sphere and K_{max} is the reciprocal-lattice vector cutoff, was originally maintained at 8.5 for all structures and volumes, corresponding to a dimension of about 100 in solving the secular equation. RK_{max} was then increased for the more sensitive total-energy calculations to 10.5, corresponding to a dimension of about 230 in solving the secular equation. The Brillouin-zone summations over the valence states in the LAPW LDA and GGA were performed with three equally spaced sets of k points: 55, 285, and 819 k points for the bcc, and 89, 505, and 1469 k points for the fcc in the irreducible $\frac{1}{48}$ of the respective Brillouin zones. We used such a dense k-point mesh to ensure that the small differences in total energy between bcc, fcc, and hcp were determined accurately. In Table I we present the energetic difference between fcc and bcc for the three different k-point meshes, solidifying the bcc structure as the ground state. For the simple cubic structure we used a mesh of 969 k points and found the total energy to be approximately 30 mRy above that of the bcc. Therefore it was not necessary to pursue a k-point convergence test for this structure.

We also checked the number of points in the logarithmic radial mesh and found that while a grid of 435 points was adequate for the LDA calculations, a 900-point grid was necessary for the GGA calculations to obtain with precision the derivative of the charge density near the nucleus.

Our LAPW total energy results were fitted to a third order polynomial using the Birch fit technique,[7] which yielded the equilibrium lattice parameter and the bulk modulus which is found from the second derivative of the total energy,

$$B = V\frac{d^2E}{dV^2}. \tag{1}$$

Additionally, we noted a point of intersection between the bcc and fcc energy curves and therefore plotted the enthalpy as a function of volume in order to check the phase transition from bcc to fcc under pressure.

B. Elastic constants

To study the mechanical stability of a cubic material, in addition to the bulk modulus, evaluation of the three independent elastic constants, C_{11}, C_{12}, and C_{44}, is needed. We summarize here the method developed in depth by Mehl and co-workers.[7,8] This is accomplished by applying appropriate strains to the crystal lattice. To determine the difference $C_{11}-C_{12}$, an orthorhombic strain e was applied in order to obtain the strained energy E in the following way:

$$E = E_0 + V(C_{11} - C_{12})e^2 + O[e^4], \tag{2}$$

where E_0 is the undistorted energy and V is the volume of the unit cell, which remains constant through the shear process. Similarly, the C_{44} elastic constant was calculated using

$$E = E_0 + \frac{1}{2}VC_{44}e^2 + O[e^4] \tag{3}$$

using a volume-conserved orthorhombic strain e. The strain energies, E, were calculated using the above equations with 1729 and 1720 k points for bcc $C_{11}-C_{12}$ and C_{44}, respectively, and with 2457 and 2329 k points for fcc $C_{11}-C_{12}$ and C_{44}, respectively. The tetragonal shear modulus, $C_{11}-C_{12}$, was calculated from the slope of the graph of E vs e^2 from Eq. (2). The elastic constants C_{11} and C_{12} themselves were then determined by combining the tetragonal shear modulus obtained from Eq. (2) with the expression for the bulk modulus,

$$B = \frac{1}{3}(C_{11} + 2C_{12}). \tag{4}$$

Using the elastic constants C_{11}, C_{12}, and C_{44} obtained from Eqs. (2)–(4), Young's modulus for this solid was calculated using the formula[9]

$$E = \frac{9BG}{3B + G}, \tag{5}$$

where B is the bulk modulus and G is the shear modulus, which cannot be calculated exactly. As such, an estimate was obtained using the Reuss (1929) modulus[9] and the Voigt (1928) modulus,[9] which are given by the following relations, respectively:

$$G_R = \frac{5(C_{11} - C_{12})C_{44}}{4C_{44} + 3(C_{11} - C_{12})}, \tag{6}$$

$$G_V = \frac{C_{11} - C_{12} + 3C_{44}}{5}. \tag{7}$$

The Reuss modulus and the Voigt modulus place lower and upper bounds on the shear modulus, respectively, such that

$$G_R < G < G_V. \tag{8}$$

An average of the two bounds was used as an educated estimate for G. This allowed the calculation of Poisson's ratio, given by the following equation:

$$\nu = \frac{3B - E}{6B}. \tag{9}$$

In order to determine the ductility of ground-state bcc radium, the Pugh[10] criterion was calculated via the following formula:

$$p = \frac{B}{G}. \tag{10}$$

The material is ductile if $p > 1.75$ and brittle if $p < 1.75$. The conditions that the bulk modulus, B, the tetragonal shear modulus, $C_{11} - C_{12}$, and the shear elastic constant, C_{44}, must all be greater than zero, were tested in order to determine the mechanical stability of bcc radium.[11]

C. Energy bands and densities of states

In the course of our study and from previous experience we realized that since only one band is occupied in this material the shape of the bands, the resulting Fermi surface, and the shape of the DOS are not sensitive to the k-point mesh used. Therefore, the energy band and density of states diagrams we present in this work were generated by our MT-APW code using 285 bcc and 505 fcc k points in the irreducible Brillouin zone. This choice is also consistent with the scattering theory of the rigid muffin-tin approximation that requires touching MT spheres as discussed in the next section. The tetrahedron method was employed to calculate the DOS for bcc and fcc radium from our converged self-consistent scalar-relativistic eigenvalues providing both the total DOS as well as the angular-momentum components of the DOS. In addition, we repeated our calculations by including the spin-orbit interaction, as will be discussed in Sec. III.

D. Superconductivity

From the density of states results at the Fermi level, we calculate, from first principles, the electron-phonon coupling constant, λ, and the superconducting transition temperature, T_c. Using McMillan's strong-coupling theory,[12] we obtain the electron-phonon coupling constant from the following formula:

$$\lambda = \frac{\eta}{M\langle\omega^2\rangle}, \tag{11}$$

where M is the atomic mass, η is the Hopfield parameter[13] calculated with the rigid-muffin-tin-approximation (RMTA),[14] $N(\epsilon_F)$ is the total density of states at the Fermi level, ϵ_F, and $\langle\omega^2\rangle$ is the square of the average phonon frequency. The Hopfield parameter is calculated from

$$\eta = N(\epsilon_F)\langle I^2\rangle \tag{12}$$

using the RMTA introduced by Gaspari and Gyorffy.[14] $\langle I^2\rangle$ is the square of the electron-ion matrix element at ϵ_F and is given by

$$\langle I^2\rangle = \frac{\epsilon_F}{\pi^2 N^2(\epsilon_F)} \sum_l \frac{2(l+1)\sin^2(\delta_{l+1} - \delta_l)N_l N_{l+1}}{N_l^{(1)} N_{l+1}^{(1)}}, \tag{13}$$

where δ_l are scattering phase shifts calculated using the self-consistent potentials generated by the energy band calculations at the MT radius of the touching spheres. $N_l(\epsilon_F)$ is the lth component of the DOS per spin, and $N_l^{(1)}$ is the free-scatterer DOS found from the radial wave functions.[15]

The LAPW total-energy results were used to determine the bulk modulus as a function of volume. These values were then used, along with the Wigner Seitz radius, to calculate the Debye temperature of the material using the following relation proposed by Moruzzi *et al.*:[16]

$$\theta_D = 131.6\sqrt{\frac{r_0 B}{M}}, \tag{14}$$

where r_0 is the equilibrium Wigner-Seitz radius in atomic units (a.u.) and B is the bulk modulus in GPa. This equation was then combined with the Debye-type approximation,

$$\langle\omega^2\rangle = \frac{1}{2}\theta_D^2, \tag{15}$$

to approximate the average phonon frequency from the volume variation in the bulk modulus. With the aforementioned information, the McMillan equation[12] gives the superconductivity transition temperature,

$$T_c = \frac{\langle\omega\rangle}{1.2}\exp\left[\frac{-1.04(1+\lambda)}{\lambda - \mu^*(1+0.62\lambda)}\right], \tag{16}$$

where μ^* is the Coulomb pseudopotential, which was was set to 0.13 in the aforementioned calculations. The effects of

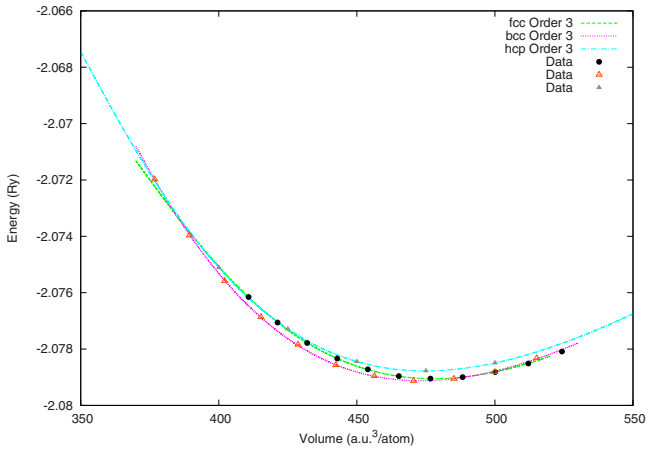

FIG. 1. (Color online) Radium GGA total energy third-order Birch fit for the bcc, fcc, and hcp structures.

varying this parameter between 0.10 and 0.16 were studied and were found not to be significant. For simplicity, in the calculation of T_c, the prefactor $\langle\omega\rangle$ was taken to be the square root of that given by Eq. (15).

III. RESULTS

A. Total energies

The results of the total energy calculations including equilibrium lattice parameters, bulk modulus, and elastic constants are shown in Table I. These results were obtained using a third-order Birch fit to the LAPW data. The LDA results incorrectly predict the fcc structure as the ground state and underestimate the measured lattice parameter of Weigel and Trinkl[17] by 5%–6% for both the MT and the full potential LAPW calculations. On the other hand the GGA results produce a lattice constant to within 1% from experiment and in addition show the ground state to be the bcc structure as shown in Fig. 1.

As discussed in our methodology section we checked very carefully the convergence of our calculations with respect to an increasing density of the k-point mesh. The fit to the LDA results gives fcc as the ground state by an extremely small energy difference. Because of the minuscule difference between the bcc and fcc total energies, the LAPW LDA was repeated with a denser k-point mesh of 285 and 505 for bcc and fcc, respectively. The fit still showed fcc as the preferred structure, but with an even smaller energy difference between bcc and fcc. The LAPW GGA total-energy results for the bcc and fcc structures were plotted as functions of volume with 55 and 89 k points, respectively, using a third-order Birch fit and predicted bcc as the ground state by a difference of about 2 mRy. The results for the denser k point meshes (285 bcc, 505 fcc, 969 sc and 819 bcc, 1469 fcc), carried out for verification that the bcc is indeed the preferred state verified the results from the first set of k points. The sc energy is significantly greater (about 30 mRy greater) than that of the bcc and of the fcc, so it is not shown. A final set of calculations was performed, however, with 819 bcc and 1469 fcc k points, $RK_{\max}$ increased to 10.5, and a denser radial mesh.

TABLE II. Calculated and experimental elastic constants of the cubic alkaline earth metals.

	Structure	$C_{11}-C_{12}$ (GPa)	C_{11} (GPa)	C_{12} (GPa)	C_{44} (GPa)	B_0 (GPa)
Calcium[a]	fcc	4	16	12	8	15
Strontium[a]	fcc	9	15	6	10	12
Barium[b]	bcc	2	9	7	13	10
Radium[c]	bcc	2.64	9.33	6.69	10.28	7.57

[a]Experiment from Ref. 18.
[b]Tight-binding from Ref. 19.
[c]LAPW results from our calculations.

These calculations included the hcp structure, which often competes with the bcc and fcc under pressure. The hcp, however, was found never to be the preferred structure in this material, as shown in Fig. 1. It achieves its ground state at $a=8.73$ bohr, $c=14.40$ bohr and, at equilibrium, it is not preferred over either the bcc or fcc. Under pressure, it achieves a lower energy than the fcc but is still not preferred to the bcc structure. Eventually, the hcp energy becomes lower than that of the bcc, but by this time, the fcc has become the preferred state, with an energy lower than both of the other two. The final run gave bcc as the preferred structure yet again, this time by an even larger energy difference. All the GGA results give bcc as the preferred equilibrium structure, in agreement with experiment.[17] Furthermore, the calculated GGA bcc equilibrium lattice parameter is in excellent agreement with experiment, overestimating by less than 1% the value obtained by Weigel and Trinkl. Furthermore, using the common tangent of the bcc and fcc curves seen in Fig. 1 or equivalently by calculating the enthalpy

$$H = E + PV. \tag{17}$$

we confirmed a phase transition from bcc to fcc at a pressure of about 2.0 GPa.

B. Elastic constants

The GGA strain energies for the bcc and fcc structures, calculated at equilibrium and subsequently used in Eqs. (2) and (3) were plotted as functions of the square of the applied strain. These results were used to determine the tetragonal shear modulus, $C_{11}-C_{12}$, from Eq. (2) and the shear elastic constant, C_{44}, from Eq. (3). The former result was then combined with the expression for the bulk modulus, Eq. (4), and the bulk modulus value at equilibrium, to determine C_{11} and C_{12} themselves. The tetragonal shear modulus, the shear elastic constant, and the bulk modulus were all found to be greater than zero, which verified the mechanical stability of the bcc structure at equilibrium, as predicted by the total-energy results. From the calculated elastic constants, Young's modulus and Poisson's ratio were calculated to further explore the mechanical properties of radium. The predicted elastic constants and bulk modulus of radium have small values similar to those of the other alkaline earth metals, as demonstrated in Table II, consistent with the high compressibility of these materials. Furthermore, we notice that the bcc

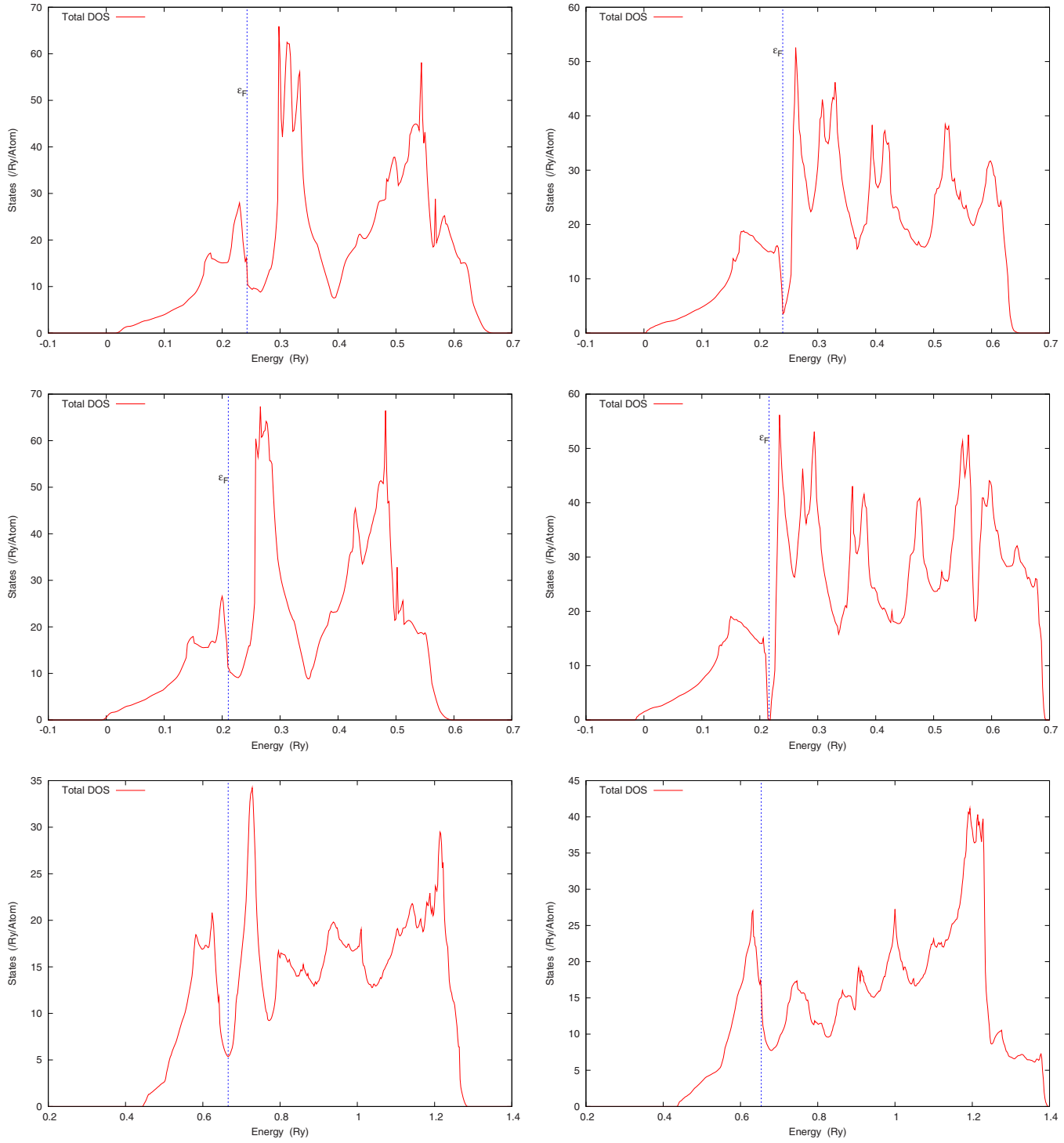

FIG. 2. (Color online) Total densities of states for bcc and fcc Radium under ambient conditions, in the expanded lattice, and under high pressure. The vertical, dash-dotted line designates the Fermi level with respect to the muffin-tin zero.

bulk modulus follows the decreasing trend established by the lighter rare earth metals. The values obtained for Young's modulus, Poisson's ratio, and the shear modulus for this material were 11.75, 0.24, and 4.73, respectively. The value obtained for the B/G was $1.60 < 1.75$, indicating that bcc radium is brittle, according to the Pugh ductility criterion.

C. Densities of states

The total and angular-momentum-decomposed densities of states for the bcc and fcc structures are shown in Fig. 2 at ambient conditions, at slightly negative pressure, and at large positive pressure. The bcc and fcc structures exhibit substantial differences in the DOS behavior at ambient and expanded lattice conditions, with the most striking difference

TABLE III. Spin-orbit band splittings in fcc radium at ambient conditions and under significant pressure. The numbers in parentheses indicate the degeneracies.

Lattice (bohr)	Symmetry direction	Energy (Ry)	Spin-orbit energies (Ry)
12.4	Γ'_{25}	0.38247 (3)	0.37721 (2)
			0.39096
	L_3	0.37011 (2)	0.36276
			0.37693
9.2	Γ'_{25}	0.87465 (3)	0.90183 (2)
			0.92369
	L_3	0.83546 (2)	0.85446
			0.87638

being that for the fcc, $N(\epsilon_F) \approx 0$, indicating semimetallic behavior. Under pressure, the strong peak in the DOS just above the Fermi level in both the bcc and fcc cases results from an increase in contribution from d states, primarily the t_{2g}. In the bcc structure, the t_{2g} contribution at ϵ_F falls greatly, causing a similar fall in $N(\epsilon_F)$ until another increase in d character, this time as a result of a significant increase in the e_g contribution. In the fcc, too, the behavior of $N(\epsilon)$ imitates that of t_{2g}, though neither decreases significantly until an energy of about 0.4 Ry, at which point both drop suddenly. However, the subsequent increase in the contribution from e_g states, as seen in the bcc structure, then takes effect, increasing $N(\epsilon)$. Comparing with the other alkaline earth metals, we note that this semimetallic behavior is absent in barium, whose ground state is the bcc structure but manifests itself in strontium as well, where fcc is the preferred structure.[20] The two structures show somewhat similar overall DOS under high pressure but differ radically in their $N(\epsilon_F)$. While in the bcc structure, $N(\epsilon_F)$ decreases by a factor of about 3 under pressure, the opposite is the case for the fcc, where we witness a strong peak in $N(\epsilon_F)$, leading to a richer Fermi surface, at an energy just below the Fermi level primarily because of spikes in the contributions of d-like components, t_{2g} and e_g. This added d character contributes greatly to the predicted superconducting properties in the fcc structure under pressure. The values of the DOS at ϵ_F are given in Table IV.

D. Band structure

The band structures of the bcc and fcc structures at ambient conditions, in the expanded lattice, and under pressure are shown in Fig. 3. Because the total energy of the material is determined primarily from the densities of states below the Fermi level, and because the DOS in this range is dominated by s states, we may safely assume spin-orbit effects to be negligible at equilibrium and at modest pressures despite the high atomic number of this material. In Sec. III E, we demonstrate in detail that spin-orbit effects are important only

TABLE IV. Fermi level with respect to the muffin-tin zero, total and angular- momentum-decomposed densities of states, Hopfield parameter, η, electron-phonon coupling, λ, and superconducting temperature, T_c.

Lattice (bohr)	Pressure (GPa)	ϵ_F	N_{tot} (states/Ry)	s (states/Ry)	p (states/Ry)	d (states/Ry)	f (states/Ry)	Eta ($\frac{eV}{A^2}$)	Lambda	T_c (K)
					bcc					
10.2	−0.701	0.212	13.704	1.311	0.991	6.551	0.225	0.145	0.379	0.042
9.8	0.054	0.244	13.595	1.391	0.928	6.378	0.261	0.241	0.420	0.116
9.4	1.255	0.283	13.737	1.410	0.935	6.332	0.298	0.373	0.451	0.221
9.0	3.112	0.330	14.554	1.540	0.974	6.616	0.349	0.628	0.542	0.674
8.6	5.928	0.389	11.510	1.105	0.871	5.122	0.292	0.750	0.471	0.393
8.2	10.127	0.460	7.945	0.731	0.546	3.597	0.256	1.044	0.487	0.548
7.8	16.288	0.550	6.142	0.591	0.471	2.636	0.248	1.197	0.424	0.275
7.4	25.133	0.666	5.381	0.475	0.428	2.253	0.302	1.588	0.441	0.402
					fcc					
12.8	−0.532	0.218	0.000	0.000	0.000	0.000	0.000	0.000	0.000	0.000
12.4	0.091	0.241	5.921	0.270	0.455	3.523	0.087	0.094	0.173	0.000
12.0	0.951	0.269	11.390	0.748	0.826	6.555	0.215	0.269	0.377	0.056
11.6	2.113	0.301	12.859	0.940	0.830	7.347	0.299	0.435	0.476	0.318
11.2	3.645	0.338	14.931	1.261	0.887	8.308	0.438	0.725	0.633	1.215
10.8	5.615	0.382	14.722	1.240	0.835	8.077	0.523	1.033	0.733	2.105
10.4	8.066	0.433	14.383	1.208	0.800	7.726	0.620	1.449	0.856	3.359
10.0	10.967	0.494	13.426	1.148	0.729	6.757	0.901	1.971	1.002	4.921
9.6	14.111	0.566	13.423	1.229	0.743	6.340	1.142	2.579	1.186	6.739
9.2	16.901	0.655	20.444	1.338	1.498	9.698	1.605	3.392	1.544	9.288

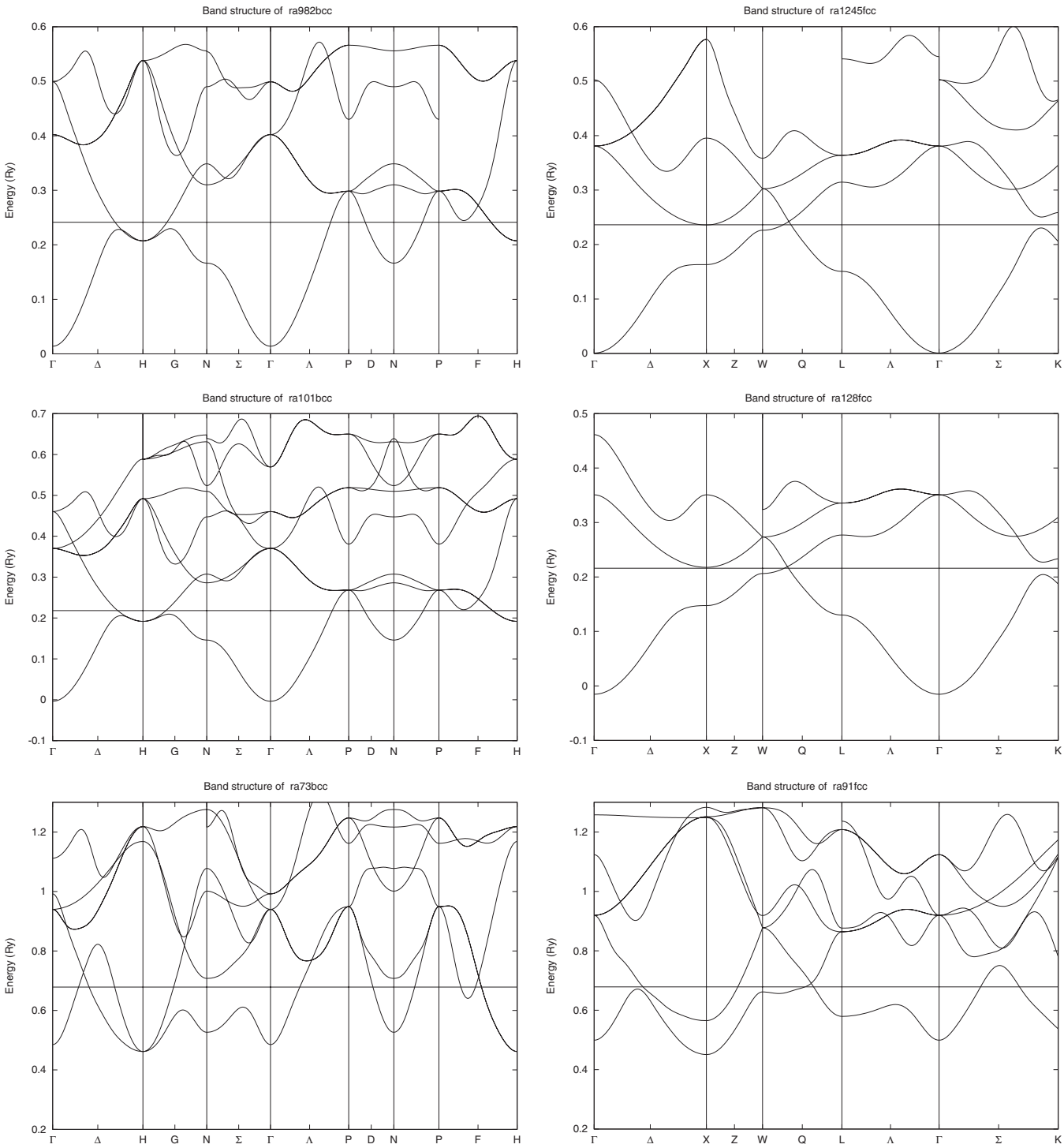

FIG. 3. Band structure of radium.

above ϵ_F. We note that in the expanded fcc lattice, the Fermi level does not cross any of the bands, but it is tangent at the symmetry point X and goes through a crossing in the Q direction, thus confirming the semimetallic behavior predicted by the DOS results at this lattice parameter. The band structure of fcc radium at ambient conditions is quite similar to that of strontium.[20] The Fermi level just barely crosses at X and just misses the crossing at Q, resulting in the very low $N(\epsilon_F)$ found in the DOS results. At higher pressures, however, we see that the upward shifting of the bands and Fermi level results in the latter's crossing many bands, creating a much larger $N(\epsilon_F)$. Specifically, the Fermi level crosses at least one band in every symmetry direction in the Brillouin zone except Λ and there exists an electron hole in the Σ direction.

For the energy bands of the bcc structure we note a clear metallic behavior unlike the semimetal features shown in the fcc lattice. The band structure of bcc for this material is almost identical for the expanded and equilibrium lattices. Furthermore, the band structure at equilibrium resembles that

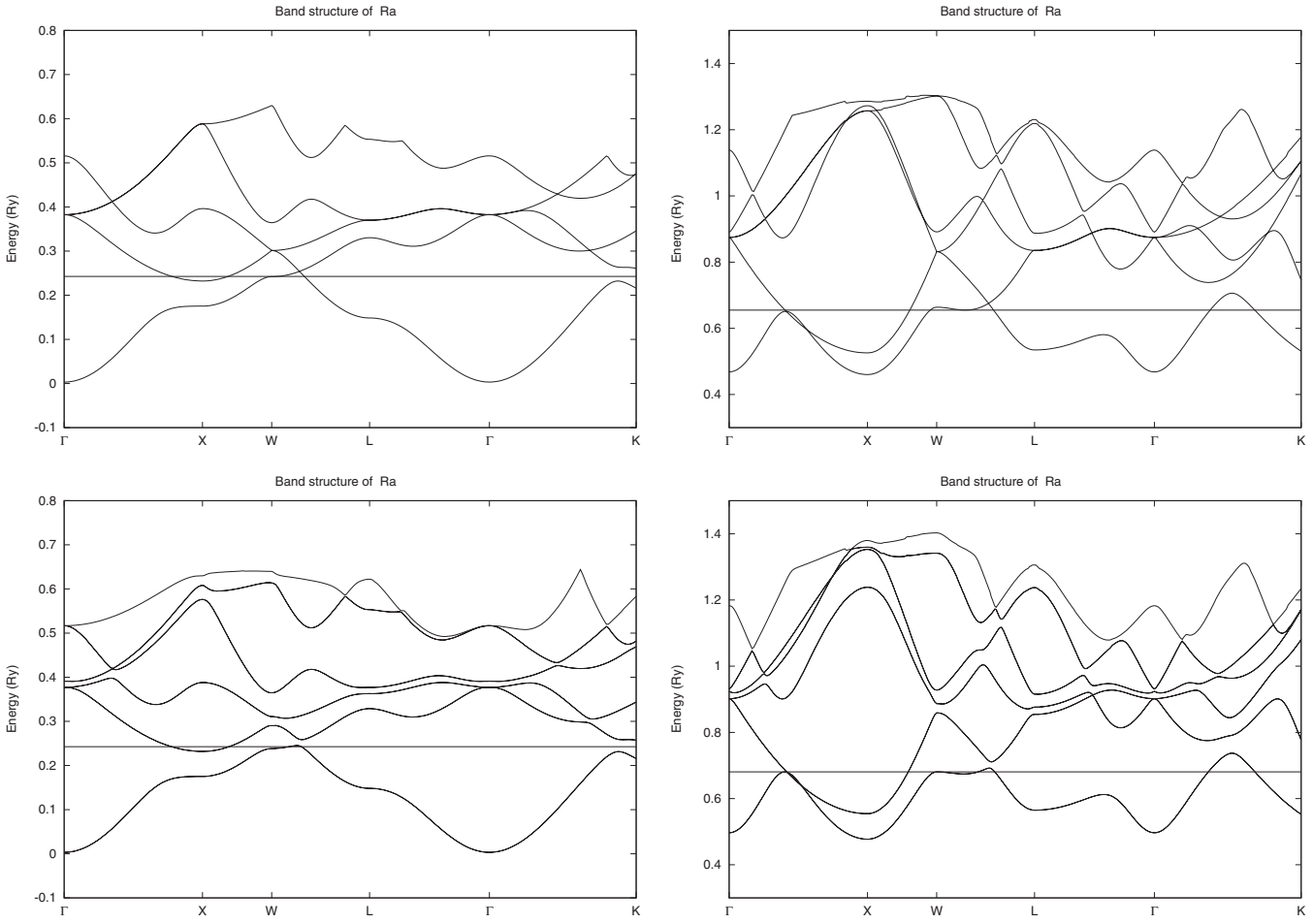

FIG. 4. Band structure of fcc radium at ambient conditions (left) and under significant pressure (right) with and without spin-orbit effects.

of Barium very closely.[20] At high pressures, however, the upward shifting of the bands and Fermi level, ϵ_F, bring about the same change as observed in the fcc lattice, namely, the crossing of many more bands by ϵ_F and, therefore, an increased $N(\epsilon_F)$ at high pressure. We observe that the Fermi level crosses at least one band in every symmetry direction in the Brillouin zone except Σ and that there exists a hole pocket in the Σ direction. Similarly to the fcc structure we notice increased d-state character near ϵ_F, which results in an increase in the electron-phonon coupling discussed in Sec. III F.

E. Spin-orbit interaction and effects

Below ϵ_F, both at ambient conditions and under moderate pressures, the densities of states consist almost entirely of s states, and spin-orbit couplings can therefore be neglected. Under significant pressure, however, it is evident that d states dominate the DOS. As a result, we explored the effects of the spin-orbit interaction in radium. The differences under ambient conditions and at low pressures were entirely negligible. Higher pressures gave rise to discernible differences, but below the Fermi level, these differences were still quite small, never exceeding 10%. Above the Fermi level, there were much more significant changes to the DOS and band structure, with several band splittings taking place. These properties, however, do not affect the parameters for superconductivity, which depend only on states at the Fermi level, and we therefore neglect spin-orbit effects in the next section. In Fig. 4, we compare energy bands with spin-orbit included versus the bands without spin orbit. It is clear that the differences show above ϵ_F. In more detail, we show in Table III how the energies at the high symmetry points Γ'_{25} and L_3 split.

F. Superconductivity

Using the results obtained from our total-energy and density-of-states calculations, we determined the necessary inputs into the McMillan equations to calculate the superconducting transition temperatures at different volumes/pressures for the bcc and fcc structures. Since the transition from bcc to fcc occurs at a relatively lower pressure of about 2.0 GPa, we will be concerned with only the fcc structure for most of the prediction of superconducting properties and present only those results graphically. From the Moruzzi formula,[16] we obtained a Debye temperature of about 53 K at equilibrium, and we made our predictions for the superconductivity transition temperature of radium using the Debye temperature corresponding to each lattice constant as given by this formula. The bulk modulus B, average phonon fre-

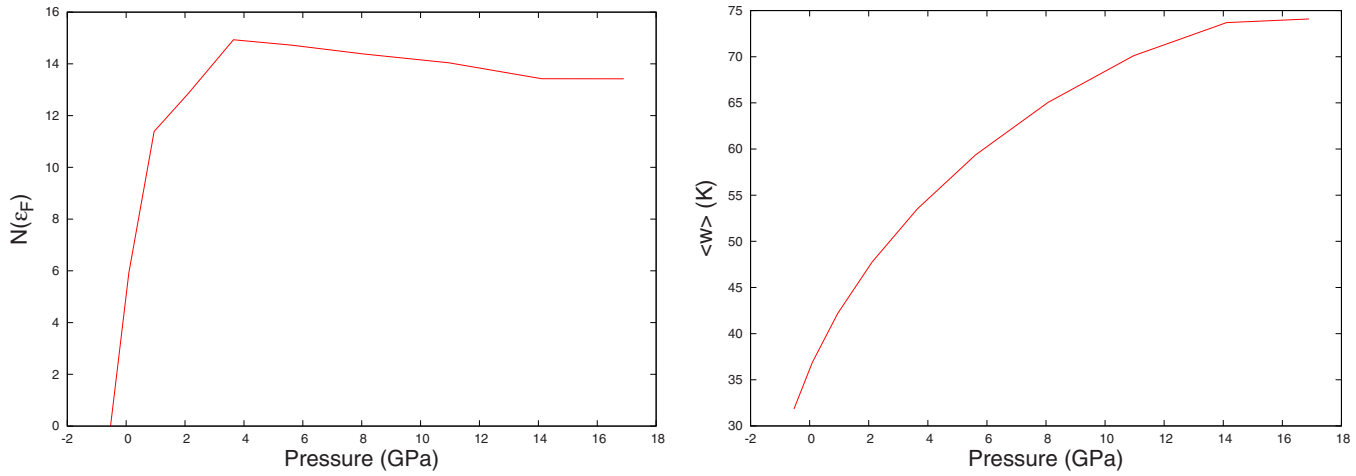

FIG. 5. (Color online) $N(\epsilon_F)$ and $\langle\omega\rangle$ of fcc radium functions of pressure.

quency, $\langle\omega\rangle$, density of states at the Fermi level, $N(\epsilon_F)$, Hopfield parameter, η, electron-phonon coupling, λ, and superconductivity transition temperature, T_c, are shown as functions of pressure in Figs. 5 and 6, respectively, using the expression for $\langle\omega\rangle$ given by Eq. (15). Furthermore, the angular-momentum-decomposed densities of states are shown in Table IV.

In the bcc structure, the combination of the decreasing total density of states at the Fermi level and the relatively modest increase in η combine to keep a fairly constant λ throughout the pressure range, resulting in only very low T_c values (Fig. 7). Therefore, the bcc structure, even if it were to remain the preferred structure, would not superconduct.

In the fcc structure, which is the preferred structure at pressures of about 2 GPa and above, we notice a different behavior of the parameters. Although $\langle\omega\rangle$ increases, $N(\epsilon_F)$ increases very rapidly, causing η and λ both to increase very rapidly, resulting in a similar increase in T_c. In this pressure range, η drives T_c. From 4 GPa to about 14 GPa, $N(\epsilon_F)$ suddenly stops its fast increase and even decreases, causing η to increase slightly less quickly than before. Meanwhile, the rate of increase in $\langle\omega\rangle$ decreases, but the net result is a slower increase in λ and, subsequently, in T_c. Finally, from 14 to 16.9 GPa, $\langle\omega\rangle$ levels off almost entirely, but $N(\epsilon_F)$ ceases to decrease and we witness a rapid increase in η, a behavior mimicked by λ and T_c, culminating in a superconducitivity transition temperature of about 9.3 K at a pressure of about 16.9 GPa. We note that η increases monotonically throughout the pressure range. It is important to realize, however, that originally, it increases as a result of the increase in $N(\epsilon_F)$ with higher pressure. The plateau (and even decrease) in $N(\epsilon_F)$ occurs at high pressures, at which point the electron-ion matrix element, $\langle I^2\rangle$, which was previously constant, begins to increase. This comes about as a result of the substantial d and f character present in the DOS at the Fermi level under high pressures, as seen in the DOS and bands and in Table IV because the d-like and f-like states are in large part responsible for the magnitude of $\langle I^2\rangle$.

It is therefore evident that the variation in T_c as a result of the changes in the input parameters to the McMillan equations, Eqs. (11) and (16), cannot be summed up by any simple, monotonic relationship with respect to any one of its parameters. From Eq. (11), it is clear that λ increases with increase in η and decreases with increase in $\langle\omega\rangle$. However, both η and $\langle\omega\rangle$ increase with pressure and it is the relative percent increases that determine the overall change in the

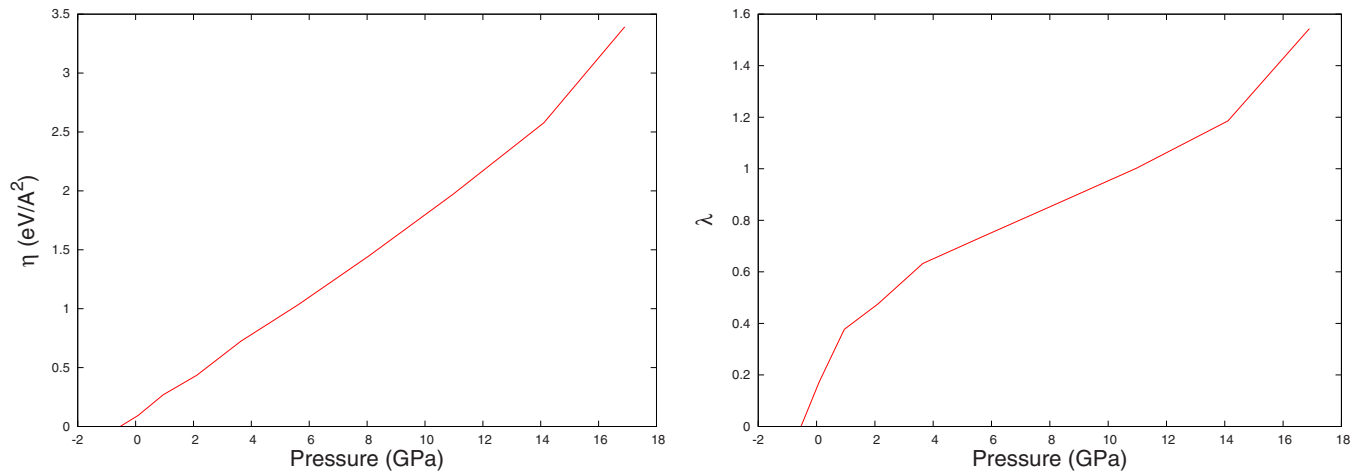

FIG. 6. (Color online) η and λ of fcc radium as functions of pressure.

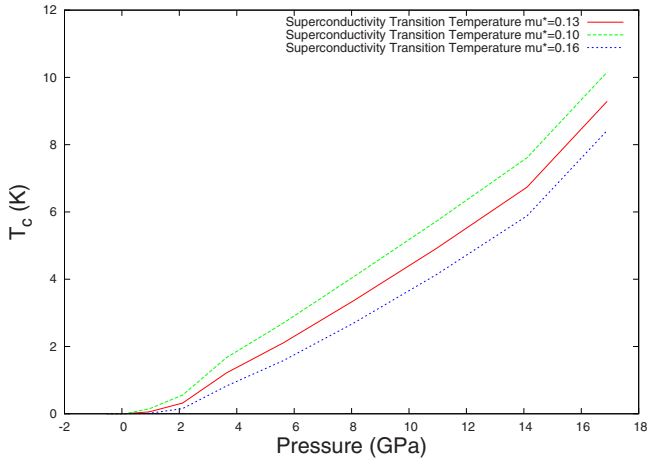

FIG. 7. (Color online) T_c of fcc radium as functions of pressure.

electron-phonon coupling, which appears in the exponent of T_c. Furthermore, $\langle\omega\rangle$ appears in the numerator of T_c, where it impacts T_c differently than when it indirectly impacts T_c via its relationship with λ. The multiple behaviors of T_c under pressure demonstrate this complex relationship. The interdependence of these parameters yields significantly different effects on T_c in different pressure ranges, as we have observed in radium. Finally, it should be mentioned that calcium, which has the same number of valence electrons as radium, has likewise been reported[22,23] from Shi *et al.*[21] to superconduct at $T_c = 15-25$ K at pressures over 150 GPa.

IV. CONCLUSIONS

In conclusion, there exists no theoretical and extremely minimal experimental previous work on the electronic structure and related properties of radium. We have performed, to our knowledge, the first set of electronic structure calculations for this material. Specifically, we studied the following: the total energies and equilibrium lattice parameters for the sc, bcc, fcc, and hcp structures; the elastic constants for bcc and fcc at equilibrium conditions; the densities of states for the bcc and fcc structures; the band structure for the bcc and fcc structures; the superconducting properties for the bcc and fcc structures at high pressures. We conclude that our LAPW GGA calculations predict the correct equilibrium structure give the equilibrium lattice constant in extremely close agreement with experiment, whereas the LAPW LDA underestimate the equilibrium lattice constant and incorrectly give fcc as the ground state structure (albeit by a very small margin). This results from the fact that the LDA is more suited for the transition metals because their electronic structures are dominated by the localized *d* electrons. We have furthermore explored the DOS and band structure of both bcc and fcc radium and have found results consistent with those known for other alkaline earth metals. Finally, we have studied, in depth, the superconducting properties of radium under pressure and have predicted a superconductivity transition temperature of about 9.3 K at a pressure of about 16.9 GPa in the fcc structure, following a phase transition from bcc to fcc at a pressure of about 2.0 GPa. We checked the effects of spin-orbit interactions and concluded that these effects are negligible below and at the Fermi level but significant well above it. We take the correct predictions of the ground-state structure and lattice constant as signs of the accuracy of the method and calculation, and an expanded application of DFT to this heavy element, in an area of the periodic table where DFT is often believed to fall short, and we believe that they lend credibility to the remainder of the results. In future work, we will apply the tight-binding method to this material in order to use it as a step to molecular dynamics simulations. We also plan to explore transitions under pressure to other crystal structures.

ACKNOWLEDGMENTS

This work was partially supported by ONR Grant No. N000140911025.

[1] P. Hohenberg and W. Kohn, Phys. Rev. **136**, B864 (1964).
[2] W. Kohn and L. Sham, Phys. Rev. **140**, A1133 (1965).
[3] J. P. Perdew and Y. Wang, Phys. Rev. B **45**, 13244 (1992).
[4] O. K. Andersen, Phys. Rev. B **12**, 3060 (1975).
[5] S.-H. Wei and H. Krakauer, Phys. Rev. Lett. **55**, 1200 (1985).
[6] L. Hedin and B. L. Lundqvist, J. Phys. C **4**, 2064 (1971).
[7] M. J. Mehl, B. M. Klein, and D. A. Papaconstantopoulos, *Intermetallic Compounds* (Wiley, London, 1994), Vol. 1.
[8] J. E. Osburn, M. J. Mehl, and B. M. Klein, Phys. Rev. B **43**, 1805 (1991).
[9] E. Schreiber, O. L. Anderson, and N. Soga, *Elastic Constants and Their Measurement* (McGraw-Hill, New York, 1973).
[10] S. F. Pugh, Philos. Mag. **45**, A23 (1954).
[11] M. Born and K. Huang, *Dynamical Theory of Crystal Lattices* (Oxford at the Clarendon Press, Oxford, 1991), Chap. 11, p. 13.
[12] W. L. McMillan, Phys. Rev. **167**, 331 (1968).
[13] J. J. Hopfield, Phys. Rev. **186**, 443 (1969).
[14] G. D. Gaspari and B. L. Gyorffy, Phys. Rev. Lett. **28**, 801 (1972).
[15] H. L. Skriver and I. Mertig, Phys. Rev. B **41**, 6553 (1990).
[16] V. L. Moruzzi, J. F. Janak, and K. Schwarz, Phys. Rev. B **37**, 790 (1988).
[17] F. Weigel and A. Trinkl, Radiochim. Acta **10**, 78 (1968).
[18] *Smithells Metals Reference Book*, 6th ed., edited by E. A. Brandes (Butterworths, London, 1983).
[19] M. J. Mehl and D. A. Papaconstantopoulos, Phys. Rev. B **54**, 4519 (1996).
[20] D. A. Papaconstantopoulos, *Handbook of the Band Structure of Elemental Solids* (Plenum, New York, 1986).
[21] L. Shi, D. A. Papaconstantopoulos, and M. J. Mehl, Phys. Rev. B **75**, 024512 (2007).
[22] S. Okada, K. Shimizu, T. Kobayashi, K. Amaya, and S. Endo, J. Phys. Soc. Jpn. **65**, 1924 (1996).
[23] T. Yabuuchi, T. Matsuoka, Y. Nakamoto, and K. Shimizu, J. Phys. Soc. Jpn. **75**, 083703 (2006).